Imaging hydrogenous materials with a neutron microscope

J. T. Cremer, M. A. Piestrup, H. Park, and C. K. Gary
Adelphi Technology Inc., 981-B Industrial Road, San Carlos, California 94070

R. H. Pantell
Department of Electrical Engineering, Stanford University, Stanford, California 94305

C. J. Glinka and J. G. Barker
Center for Neutron Research, National Institute for Standards and Technology, Gaithersburg, Maryland 20899

(Received 10 May 2005; accepted 18 August 2005; published online 14 October 2005)

Magnified images of materials containing hydrogen, for which the main contrast mechanism for neutrons is incoherent scattering, have been obtained using a microscope employing a neutron compound refractive lens (CRL). The CRL was composed of 100 MgF_2 biconcave lenses that produced magnified ($22.5\times$) images of polyethylene and polypropylene (hydrogen-rich) grids and biological specimens using 8.5 Å cold neutrons with a 10% bandwidth. For hydrogenous materials, 98%–99% of the attenuation is by incoherent scattering and 1%–2% from neutron absorption by the hydrogen nuclei. The small angle of acceptance of the CRL discriminates against scattered neutrons from the hydrogenous object, thereby producing the needed contrast for imaging. © *2005 American Institute of Physics*. [DOI: 10.1063/1.2089172]

Incoherent scattering is nearly isotropic and dominates in hydrogen, which by far has the strongest incoherent scattering cross section of all the elements.[1] Incoherent scattering can blur ordinary neutron radiographic images. However, incoherent scattering can be used as a contrast mechanism for neutron imaging with an optic whose angular acceptance is small. Such an optic is the compound refractive lens (CRL), which consists of a series of N biconcave lenses whose total focal length $f=f_o/N$, where f_o is the focal of one of the unit lenses. Like an ordinary optical lens, the CRL can be used for imaging by placing it between an illuminated object and a detector. The lens formula, $1/f=1/o+1/i$, where o is the distance between the CRL and the object and i is the distance between the CRL and a neutron detector.[2–5] The magnification is given by $M=i/o$, as in ordinary optics. Also, the CRL acts like a cylinder with a limited angular acceptance, $2r_a/t$, where $2r_a$ is the absorption aperture of the CRL and t is the total length of the stack of N unit lenses.

Desirable materials for a CRL are those that have a large coherent cross section to achieve large decrements in index of refraction, but also have small absorption and incoherent cross-sections to minimize attenuation of the beam through the CRL. Ideally, the material should be of uniform density so that all the strong coherent scattering remains in the forward "null" scattering direction. Materials having high purity (to avoid formation of second phase precipitates) and free from voids are required. At shorter wavelengths, Bragg coherent scattering can also cause significant attenuation. Amorphous materials (e.g., Teflon in amorphous form) or single crystals (e.g., MgF_2) are those for which the resultant coherent scattering length can be large, the incoherent scattering and absorption cross sections minimal, and Bragg scattering can be eliminated. The motion of atoms as the neutron is transmitted through the material also causes coherent phonon scattering. Materials with high atomic bond energies, or those cooled cryogenically, can reduce the amount of attenuation by phonons.

Since biological material is composed of hydrocarbons, radiographs have extensive blurring and very poor resolution due to scattered neutrons reaching the detector. A neutron microscope, using a CRL with its tight collimation, will image the paraxial trajectory neutrons that are transmitted through the sample. Thus, the CRL can provide higher resolution images than radiographs.

Biconcave lenses made from single crystal MgF_2 have been used as neutron CRLs,[6,7] Lens materials are selected based on their index of refraction, absorption, coherent, and incoherent scattering.[1,8,9] The index of refraction $n=1-\delta+i(\lambda/4\pi)\mu$ of a lens material as a function of neutron wavelength λ determines the CRL refractive and absorptive properties. The CRL atom density ρ and the bound neutron coherent scattering length b determine the refractive decrement $\delta=\lambda^2 b\rho/2\pi$, and the associated coherent scattering cross section[10,11] $\sigma_c=4\pi b^2$. The sum of the CRL neutron absorption cross section σ_a and scattering cross section σ_s yield its linear attenuation coefficient, $\mu=\rho(\sigma_a+\sigma_s)$.

The decrement δ determines the CRL focal length, $f=R/2N\delta$, and the linear attenuation μ determines the limiting absorption aperture radius, $r_a=\sqrt{4f\delta/\mu}$, where R is the radius of curvature of each of the N lenses. At the absorption aperture radius the neutron intensity is reduced by a factor e^{-2} because the biconcave lens thickness increases with distance from the CRL center axis. Spherical aberration,[12] which leads to a loss of resolution but not intensity, occurs

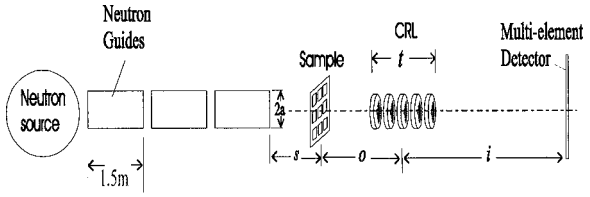

FIG. 1. Imaging experiment carried out at the NG-7 beamline. Neutron guides are removed to change the distance to guide system output, which acts as an effective source.

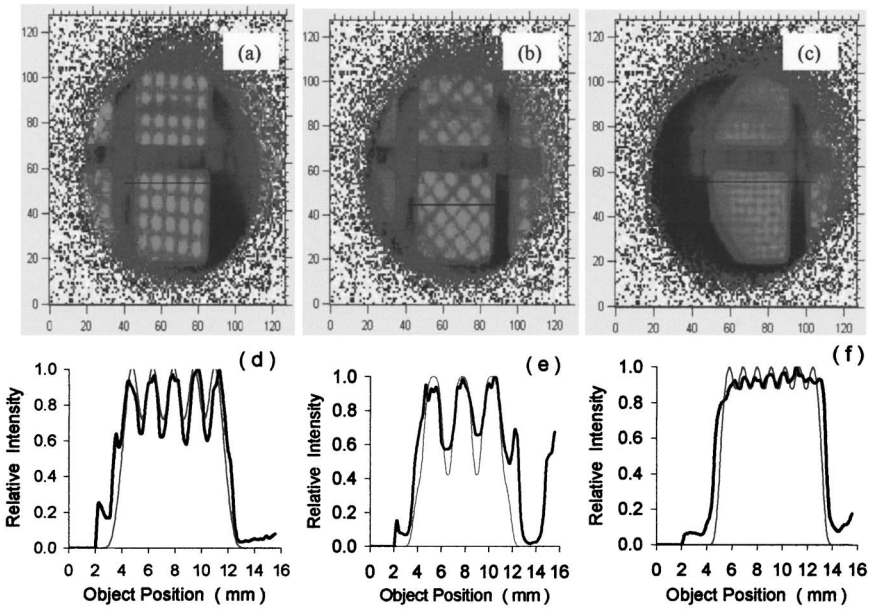

FIG. 2. The 100-lens MgF_2 CRL neutron images at 8.5 Å and 300 sec exposure images of (a) mesh #1, polypropylene square grid, (b) mesh #2, polyethylene grid, and (c) mesh #3, polypropylene square grid. Along indicated lines in (a)–(c) are normalized line profiles of measured intensity (thick curve) and theoretical intensity (thin curve) for (d) mesh #1, (e) mesh #2, and (f) mesh #3. Mesh dimensions are in Table I.

for neutrons incident outside of the parabolic aperture radius r_p of the spherical lens where $r_p=(2R^3\lambda/N\delta)^{1/4}$.

The scattering cross section σ_s in a CRL or a sample is the sum of the incoherent scattering σ_{inc} from individual atoms by the neutron wave, small-angle scattering (SAS) σ_{sas} from voids or other inhomogeneities in material, the thermal diffuse scattering σ_{phon} from lattice vibrations (phonons),[13] and possibly, elastic Bragg scattering σ_{Bragg}; i.e., $\sigma_s=\sigma_{\text{inc}}+\sigma_{\text{sas}}+\sigma_{\text{phon}}+\sigma_{\text{Bragg}}$. Double Bragg scattering and SAS are forward directed within a small cone angle, both of which lead to blurring or loss of image resolution. The isotropic scattering of incoherent scattering and thermal diffuse phonon scattering leads only to a reduction of intensity. For single crystal MgF_2, the Bragg condition can be avoided and the cross sections of single atom incoherent scattering are relatively small compared to neutron absorption.

The major contrasting mechanisms that allow neutron imaging of various samples including biological specimens are neutron absorption and the isotropic scattering (single atom incoherent and lattice vibration). Both the absorption and scattering vary across the sample, depending on sample density and composition. A hydrogenous sample that is amorphous and noncrystalline has incoherent neutron scattering accounting for 98%–99% of the neutron attenuation, whereas neutron absorption by hydrogen accounts for 1%–2%. In general, other elements have incoherent scattering cross section that are much smaller than, or at most approximately equal to, their neutron absorption cross section,[1] although atom thermal motion can increase their total scattering cross section σ_s.

The imaging experiments were performed at the NCNR on the NG-7 30-meter Small-Angle Neutron Scattering instrument.[14] Figure 1 shows the neutron microscope experimental apparatus that consists of five main elements: the neutron source, neutron guide, specimen, CRL, and detector. The exit of the rectangular neutron guide tube acted as a 50 mm$\times$50 mm uniform source of 8.5 Å neutrons that are monochromatized to a 10% bandwidth. This 8.5 Å source produces an incident flux of 3×10^4 n/mm^2/s at a sample position 1.22 m downstream.

The MgF_2 CRL in our experiment consisted of $N=100$ spherical biconcave lenses of single crystal MgF_2 fabricated by ISP Optics of Irvington, NY. Each individual spherical MgF_2 lens had a physical aperture diameter $2r_m=8.0$ mm with radius of curvature $R=8.0$ mm, minimum center thickness $d=1.0$ mm, and edge thickness 3.14 mm. The CRL total length is $t=315$ mm. Based on tabulated values[1] of scattering lengths for Mg and F, MgF_2 has a calculated decrement $\delta=5.78\times10^{-5}$. From transmission measurements the linear attenuation coefficient μ for MgF_2 at $\lambda=8.5$ Å is 5.1×10^{-3} mm^{-1} at $T=293$ K, and 1.4×10^{-3} mm^{-1} at $T=77$ K. At room temperature, the attenuation of neutrons in MgF_2 is dominated by lattice vibrations (phonons) where nearly 75% of the attenuation is by phonons. At 8.5 Å the MgF_2 CRL has absorption aperture radius $r_a=5.6$ mm and parabolic aperture radius $r_p=0.6$ mm.

This MgF_2 CRL is a thick lens[15] with a thick lens focal length 747 mm at 8.5 Å that corresponds to a thin lens approximated focal length 692 mm. The CRL image distance was set to $i=17.5$ m for maximum magnification $M=22.5$, and the object distance was accordingly set to $o=0.78$ m (measured CRL center) via the lens formula, corresponding to thick lens focal length $f=747$ mm. All guides were in place with guide exit (source) to sample (object) distance $s=1.22$ m. This resulted in a field of view[5] (FOV) for the MgF_2 CRL microscope of 24.4 mm. The neutron images were recorded by a position-sensitive, multi-element ^{3}He detector array of 128$\times$128 pixels, each 5 mm$\times$5 mm in area.

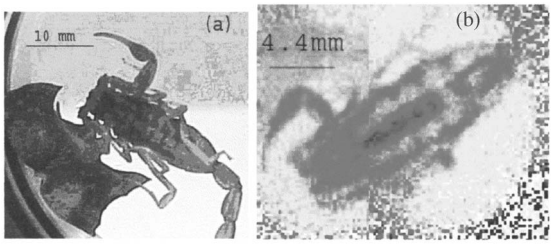

FIG. 3. (a) Photograph shows scorpion and leaf. (b) Neutron image of scorpion made from two stitched partial scorpion images at 10.0 Å and 300 sec exposure with $\times$22.5 magnification.

TABLE I. Mesh material, dimensions, and transmission fraction.

	Material	Hole dimension In mesh	Filament width	Filament thickness	Transmission fraction
Mesh #1	polypropylene	0.76 mm × 0.94 mm	0.63 mm	0.91 mm	0.44
Mesh #2	polyethylene	1.52 mm × 1.52 mm	0.51 mm	1.14 mm	0.36
Mesh #3	polypropylene	0.76 mm × 0.94 mm	0.36 mm	0.36 mm	0.72

The pixels are arranged in a square matrix covering an area 640 mm × 640 mm that can be positioned at any distance between 3.2 m to 17.5 m downstream of the CRL.

The two-dimensional detector image of the sample was normalized relative to the corresponding image with no sample to eliminate nonuniformities in the neutron beam. The measured spatial resolution of a detector pixel σ_{id} is Gaussian in shape, with full width at half maximum (FWHM) of 5.0 mm. The detector object resolution $\sigma_{od}=\sigma_{id}/M$ is limited to 222 μm with $M=22.5$. The effective aperture radius $r_e=4.0$ mm is the minimum of physical aperture radius $r_m=4.0$ mm and absorption aperture radius $r_a=5.6$ mm at $\lambda=8.5$ Å. The CRL Rayleigh-limited object resolution, $\sigma_R=0.61\lambda o/r_m$ for object distance $o=0.78$ m and aperture radius $r_m=4.0$ mm, is $\sigma_R=0.1$ μm at 8.5 Å. The chromatic aberration-limited object resolution is $\sigma_c=(2r_m(1+M)/M)(\Delta\lambda/\lambda)$. For the MgF_2 CRL with bandwidth $\Delta\lambda/\lambda=0.1$ the chromatic aberration is 835 μm. Thus, the imaging system resolution $\sigma_{tot}=864$ μm, where $\sigma_{tot}^2=\sigma_R^2+\sigma_c^2+\sigma_{od}^2$, is dominated by chromatic aberration.

Three plastic meshes of fine and coarse polyethylene and polypropylene grids, as well as biological specimens (preserved scorpion and leaf), were used as objects in an imaging experiment with cold neutrons. The biological samples may exhibit some blurring from SAS, but the plastic meshes should not exhibit blurring from SAS or double Bragg scattering. Table I lists the three mesh samples, including their approximately rectangular filament and open hole dimensions, and the minimum transmission fraction through the mesh filaments. Based on transmission measurements made on separate samples, the linear attenuation coefficient for polyethylene and polypropylene is estimated to be 0.9 ± 0.1 mm^{-1} at $\lambda=8.5$ Å.

The top three pictures in Figs. 2(a)–2(c) are linear scale, false color neutron images of the grids taken with 8.5 Å wavelength neutrons in a 300 s exposure. The scale on the false color neutron images is the detector pixel number with 20 pixels per scale division. The detector pixel to pixel center spacing is 5 mm. The meshes were mounted on a cadmium sheet with 10 mm × 10 mm square holes. The wide, dark horizontal, and vertical bands in Figs. 2(a)–2(c) correspond to the cadmium slats.

Below in Figs. 2(d)–2(f) are normalized line intensity profiles taken along horizontal lines shown in Figs. 2(a)–2(c). In each figure are the measured object line intensity profile (thick curve) and the calculated object line intensity profile (thin curve) along the indicated line. The calculated object line intensity profile is obtained by convolution of the mesh attenuation profile (via Table I mesh dimensions and transmission fractions) with the detector system resolution, a Gaussian profile with FWHM, $\sigma_{tot}=864$ μm. The filament minimum transmission fractions are 0.44 in Fig. 2(d), 0.36 in Fig. 2(e), and 0.72 in Fig. 2(f), and are dependent on filament thickness and material composition.

The image intensity profile FWHM yield the approximate gap and filament dimensions of the polypropylene meshes. For example in Fig. 2(a), the neutron image of the coarse propylene mesh has a measured FWHM gap width of 20 mm between adjacent vertical filaments. This measured neutron image gap width, divided by magnification $M=22.5$, yields a measured object gap width 0.88 mm as compared to the actual 0.76 mm.

With the same setup used with the plastic grids, we imaged a preserved scorpion and leaf at 10.0 Å in a 300 sec exposure time. Figure 3(a) shows a photo of the scorpion and a leaf with a superimposed 10 mm scale. Figure 3(b) shows a stitched neutron image of the scorpion with the leaf removed and the scorpion reoriented. The limited 24 mm CRL FOV required stitching two partial scorpion neutron images at 10.0 Å and 300 sec as shown in Fig. 3(b), and is displayed with a superimposed 4.4 mm scale. This linear scale neutron image of the scorpion shows a variation in density, indicating some areas of the scorpion contain more hydrogen than others.

This work was supported in part by U.S. Department of Energy and U.S. Institutes of Health (Grants DE-FG02-03ER83862 and IR43 CA115248). The authors thank Bryan Greenwald at the Center for Neutron Research, National Institute for Standards and Technology (NIST) for technical assistance. Certain commercial materials are identified in this paper to foster understanding. Such identification does not imply recommendation or endorsement by NIST, nor the materials or equipment identified are necessarily the best available for the purpose.

[1]NIST Center for Neutron Research, Neutron Scattering Lengths and Cross Sections.
[2]H. R. Beguiristain, I. S. Anderson, C. D. Dewhurst, M. A. Piestrup, J. T. Cremer, and R. H. Pantell, Appl. Phys. Lett. **81**, 4290 (2002).
[3]H. R. Beguiristain, J. T. Cremer, and M. A. Piestrup, U.S. Patent No. US 6 674 583 B2, 6 January 2004.
[4]M. A. Piestrup, R. H. Pantell, and H. R. Beguiristain, U.S. Patent No. US 6 765 197 B2, 20 July 2004.
[5]J. T. Cremer, M. A. Piestrup, C. K. Gary, R. H. Pantell, and C. J. Glinka, Appl. Phys. Lett. **85**, 494 (2004).
[6]M. R. Eskildsen, P. L. Gammel, E. D. Isaacs, C. Detlefs, K. Mortensen, and D. J. Bishop, Nature (London) **391**, 563 (1998).
[7]S. M. Choi, J. G. Barker, C. J. Glinka, Y. T. Cheng, and P. L. Gammel, J. Appl. Crystallogr. **33**, 792 (2000).
[8]Los Alamos National Laboratory, T-2 Nuclear Information Service.
[9]Brookhaven National Laboratory, Computer Index of Nuclear Reaction Data (CINDA).
[10]V. F. Sears, *Neutron Optics* (Oxford University Press, New York, 1989).
[11]G. L. Squires, Thermal Neutron Scattering (Dover, Mineola, 1978).
[12]J. T. Cremer, M. A. Piestrup, C. K. Gary, H. Park, and R. H. Pantell, Proc. SPIE **5541**, 75 (2004).
[13]A. K. Freund, Nucl. Instrum. Methods Phys. Res. **213**, 495 (1983).
[14]C. J. Glinka, J. G. Barker, B. Hammouda, S. Krueger, J. J. Moyer, and W. J. Orts, J. Appl. Crystallogr. **31**, 430 (1998).
[15]R. H. Pantell, J. Feinstein, H. R. Beguiristain, M. A. Piestrup, G. K. Gary, and J. T. Cremer, Appl. Opt. **42**, 4 (2003).